Effects of confinment in the buckling of a flexible plate in axial flow: experimental and numerical study

Julie Adjiman, Olivier Doaré, Pierre Moussou, Nicolas de Buretel de Chassey

EFFECTS OF CONFINMENT IN THE BUCKLING OF A FLEXIBLE PLATE IN AXIAL FLOW: EXPERIMENTAL AND NUMERICAL STUDY

Julie Adjiman
IMSIA
UMR CNRS EDF CEA ENSTA 8193
Palaiseau, 91120
France
Email julie.adjiman@ensta-paristech.fr

Olivier Doaré
IMSIA
UMR CNRS EDF CEA ENSTA 8193
Palaiseau, 91120
France
Email olivier.doare@ensta-paristech.fr

Pierre Moussou
EDF Lab Paris-Saclay
Palaiseau, 91120
France
Email pierre.moussou@edf.fr

Nicolas De Buretel De Chassey
EDF Lab Paris-Saclay
Palaiseau, 91120
France

ABSTRACT

Static instability of flexible structures forced by a parallel flow, a.k.a. divergence, has been the subject of a relatively small amount of studies, unlike flutter. In order to prepare future studies of the collective behaviour of several slender structures coupled by the fluid in axial flow, the canonical case of a flat flexible plate clamped at both ends is investigated numerically and experimentally. The onset of divergence is determined throughout a series of calculation of the fluid forces generated by a prescribed deformation of the plate. Using the Galerkin method, these fluid forces are expanded in the basis of the natural modes; they exactly balance the mechanical forces when the fluid velocity reaches the instability threshold. The instability velocity can be determined by an eigenvalue calculation involving the fluid force expansion and the modal stiffnesses of the plate. Comparisons are provided with 2D analytical calculations and with an experiment performed with a 0.3m×0.03m mylar plate at Reynolds numbers varying between 10^4 and 10^5. A fair agreement is observed between the 3D potential calculation and the experiments, whereas the 2D analytical solution underestimates the instability velocity.

NOMENCLATURE

C plate-to-wall distance along the y axis
D plate-to-wall distance along the z axis
E Young modulus of the plate
H plate's width
h_p plate's thickness
K_n wavenumber associated to the n-th mode of the plate
L plate's length
p fluid pressure
U inlet fluid velocity
ν Poisson ratio
Φ potential function associated to the fluid flow
ρ volumic mass of the fluid

INTRODUCTION

A slender structure slightly deformed and placed in an axial flow is submitted to fluid forces increase the deformation. These fluid forces, depending on the incoming fluid velocity, can overcome the rigidity forces and lead to different types of deformation of the structure: for static deformations, this instability phenomenon is known as divergence or buckling, and as flutter for dynamic deformations. For structures fixed or clamped at both ends, divergence or buckling occurs before flutter [1]. In this paper, the aim is to obtain the divergence velocity for the case of a single flexible plate confined in an axial flow with clamped-clamped boundary conditions. At the onset of divergence, the fluid and structure forces are exactly equal, and if a small perturbation is applied to the structure (in the form of a natural mode shape for example), the structure remains deformed in a marginal equilibrium state . To compute numerically the critical velocity, a direct static method is proposed and implemented. The influence of the geometry parameters on the critical velocity is then adressed, with a comparison between the results given by 2D and 3D calculations.

FLEXIBLE PLATE IN A CONFINED AXIAL FLOW

A plate of length L and width H is placed in a rectangular channel of dimensions $H+2C$ and $2D$ as sketched in figure 1. If the plate undergoes a lateral deflection $\zeta(x)$ due to an external forcing f_{ext}, the linearized plate equation comes down to:

$$\frac{Eh_p^3}{12(1-\nu^2)}\left(\frac{\partial^2}{\partial x^2}+\frac{\partial^2}{\partial z^2}\right)^2\zeta = f_{ext}, \qquad (1)$$

Proceedings of the 11th International Conference on Flow Induced Vibration and Noise. The Hague, The Netherlands. 4-6 July 2016

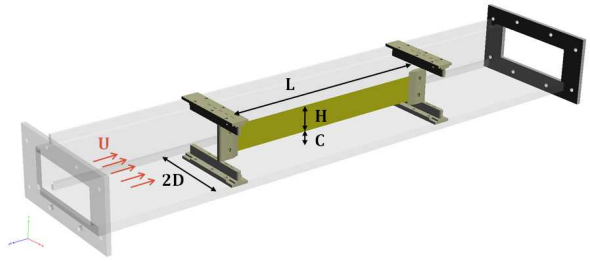

FIGURE 1. Notations

where ν and E are respectively Poisson's ratio and Young's modulus of the plate, and h_p is the plate's thickness. Expanding this equation in the natural modes basis is a widespread technique ([2], [1], [3]) and is used here to obtain a matricial form of the equilibrium:

$$\frac{Eh_p^3}{12(1-\nu^2)}\mathbf{K_4}\mathbf{V} = \mathbf{F_{ext}} \tag{2}$$

where $\mathbf{K_4}$ is the rigidity matrix with only diagonal terms $(K_nL)^4$ with K_n the wavenumber associated to the n^{th} mode of the plate; and $\mathbf{V}$ is the array build on the modal displacements of the plate q_p.

For a statically deformed plate in an axial flow, a force distribution is generated due to the differences in the pressure field near both sides of the plate. This external forcing is due to the pressure forces which can be computed in the whole fluid domain in the context of a potential flow with the help of the Bernoulli equation:

$$p = -\rho U\frac{\partial \Phi}{\partial x} \tag{3}$$

As any deformation of the plate can be written as $\zeta(x,t) = \sum_n q_n\xi_n$ where ξ_n is a natural mode with clamped-clamped conditions, the potential can be expanded in similar terms:

$$\Phi = U\sum_n q_n\varphi_n \tag{4}$$

The term φ_p corresponds to the fluid potential around a deformed plate with a deflection $q_p\xi_p$ proportional to the plate's p^{th} natural mode shape ξ_p with an amplitude q_p. Each φ_p satisfies the Laplace equation with the same boundary conditions on the plate and on the channel walls(no penetration of the flow).

It is assumed that the derivatives of the potential above $(+)$ and below $(-)$ the plate can be expanded in the basis of the plate's natural modes as well:

$$f_p = \rho U^2\frac{q_p}{L}\sum_n H_{pn}\xi_n,$$
$$\text{where } H_{pn} = \frac{L}{\int \xi_n^2 ds}\int \frac{\partial}{\partial x}(\varphi_p^+ - \varphi_p^-)\xi_n\, ds. \tag{5}$$

This equation highlights the fact that the fluid forces, due to a modal deformation ξ_p, generate secondary deformations involving other modes. In mathematical terms, the onset of static instability is associated to a non-vanishing solution of the exact balance between fluid and rigidity forces in the fluid-structure equation. This marginal equilibrium is written in the natural modes basis:

$$\frac{1}{12(1-\nu^2)}\frac{E}{\rho U^2}\frac{h_p^3}{L^3}(K_nL)^4 q_n = \sum_p H_{pn}q_p \tag{6}$$

Equation (6) is transformed into a matrix equality:

$$\frac{1}{12(1-\nu^2)}\frac{E}{\rho U^2}\frac{h_p^3}{L^3}\mathbf{V} = \mathbf{K_4^{-1}}\mathbf{H}\mathbf{V} \tag{7}$$

The critical non-dimensional velocity can be seen as the solution of an eignevalue problem: divergence occurs when the velocity U is such that there is a non-trivial solution to equation (7), *i.e.* when

$$U\sqrt{\rho\frac{L^3}{h_p^3}\frac{12(1-\nu^2)}{E}} = \sqrt{\frac{1}{eigenvalues(\mathbf{K_4^{-1}}\mathbf{H})}} \tag{8}$$

NUMERICAL COMPUTATION OF THE FLUID FORCES AND CRITICAL VELOCITY

The fluid problem is solved numerically for a 3-dimensional geometry. The plate has a small thickness in the geometry model, in order to provide a more realistic configuration. The plate is enclosed in a 'fluid box'; at the inlet, the velocity profile is uniform and at the outlet, the condition $\Phi = 0$ is applied since the potential problem is solved within a constant. On the channel walls, an ideal slip condition is applied. The plate's deformed profile is directly included in the geometry, allowing to solve the fluid problem for any shape, in particular for a natural mode shape. The mesh is refined in the length and width directions of the plate, in order to discretize with a good accuracy the modes up to the fifth order. The mesh of the fluid domain is entirely built with hexahedra cells, providing regularity in the resolution of the potential field (see figure 2).

The global resolution of the problem consists in: first, computing the potential field and the pressure forces for each configuration of the plate in every n^{th} mode shape; then building the matrix of interaction between the fluid and the structure by expanding the fluid forces on the natural modes basis; finally, finding the eigenvalues of $\mathbf{K_4^{-1}}\mathbf{H}$ and obtaining the non-dimensional critical velocity.

Figure 8 shows the pressure distribution obtained with a numerical simulation with *Code_Aster* [4] above and below a plate deformed in a first mode shape with a small amplitude. This pressure distribution is non-uniform in the width direction

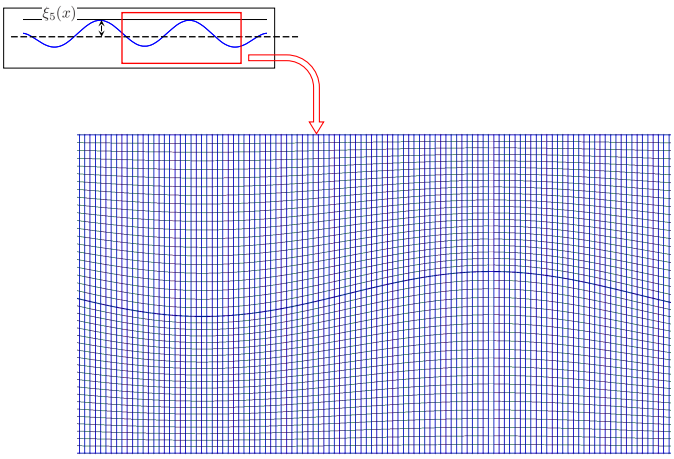

FIGURE 2. Detail of the mesh generated in the fluid domain near the plate deformed with a 5^{th} mode shape $\xi_5(x)$

FIGURE 3. Dimensionless pressure on the upper side of the plate with a first mode shape and profile of the inlet velocity

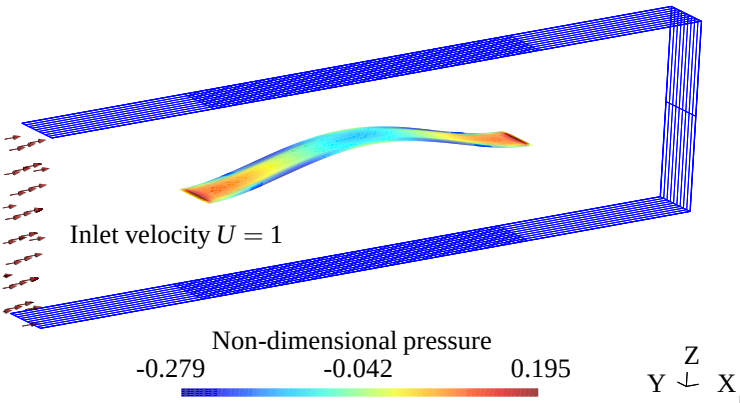

of the plate, showing that 3D effects occur near the lateral edges of the plate. Both ends of the plate are a singularity for the fluid; therefore the pressure distribution is truncated before the numerical discrete expansion on the natural modes basis.

EXPERIMENTAL SET-UP

An experimental set-up is built in order to explore configurations close to the numerical simulations. Therefore, a flexible Mylar sheet is used with the following characteristics: thickness $h_p = 250\mu m$, Young modulus $E = 5.2$ GPa, Poisson coefficient $\nu = 0.38$, length $L = 0.226$ m, width $H = 0.03$ m. In order to perform clamped-clamped boundary conditions, a streamlined piece is attached to both ends of the plate with crossing screws; the assembly is inserted and centered in a rectangular box made of transparent Plexiglas (inner dimensions: 0.04 m x 0.10 m). A fan with a honeycomb grid is connected to the box, which allows a uniform steady flow from 0 up to 50 m/s, measured with a Pitot tube at the center of the box. A laser sensor is used to measure the deflection of the plate locally, giving access to the plate's shape and amplitude of deformation.

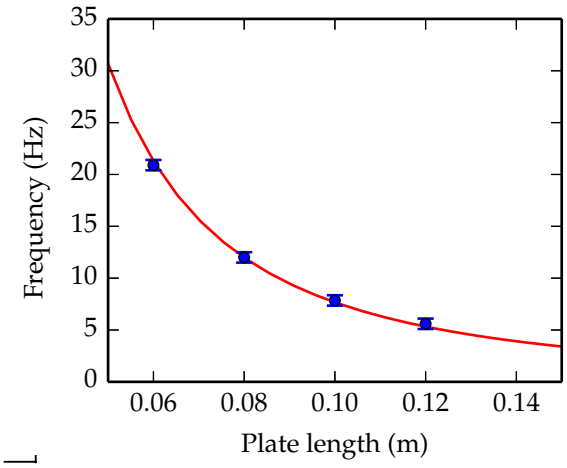

FIGURE 4. Mechanical characterization of the plate in a clamped-free configuration. Blue dots: experimental points, red line: theoretical values obtained with manufacturer's values of the plate's characteristics.

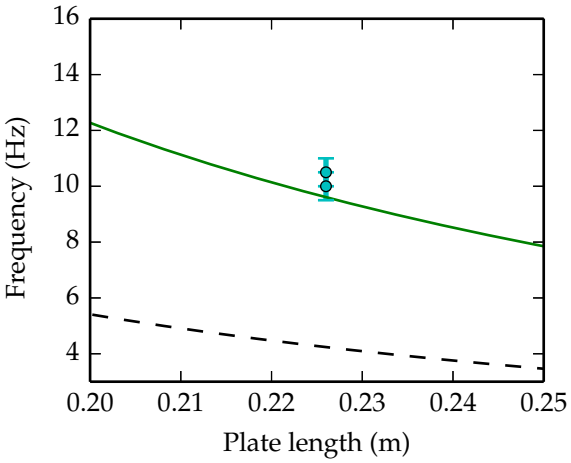

FIGURE 5. Characterization of boundary conditions. Blue dots: experimental points, solid line: theoretical values in a clamped-clamped configuration, dotted line: theoretical values in a pinned-pinned configuration.

Figure 4 shows the mechanical behaviour of the plate obtained with the response of the plates to a vibration test in clamped-clamped conditions. The displacement of the plate's free end did not exceed 10 mm; in this range, the behaviour of the plate is linear and elastic, and its natural frequency follows the theoretical law of evolution with the plate's length as in [5]. In figure 5, the natural frequency of the plate is obtained with an experimental modal analysis: the vibration of the plate is recorded after a small impact on it, and the frequency of the first flexural mode is measured on the spectrum of the response. The results allow to consider that the actual boundary conditions are close to theoretical clamped-clamped boundary conditions, and quite far from pinned-pinned boundary conditions.

In figure 6 the static profile of the plate has been recorded by by moving the laser sensor along the plate and pointing at

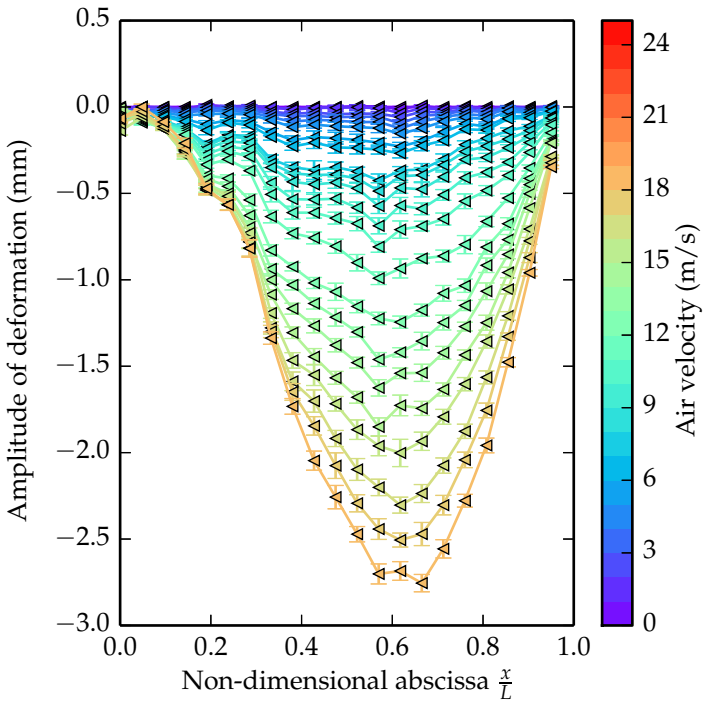

FIGURE 6. Profiles of the plate under axial flow for air velocities from 0 to 25 m/s (blue to red lines)

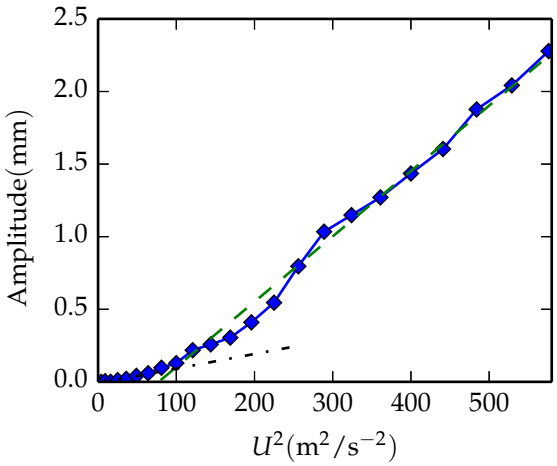

FIGURE 7. Evolution of the amplitude of deflection with flow velocity. Blue diamonds: experimental values. Black dash dotted line: linear regression at low flow velocities. Green dashed line: linear regression after divergence.

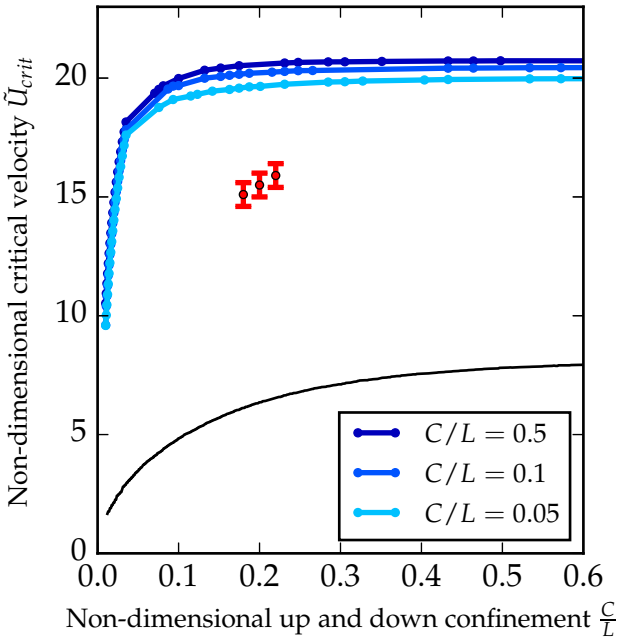

FIGURE 8. Evolution of the dimensionless critical velocity with lateral confinment for $\frac{C}{L} = 0.05, 0.1, 0.5$. Blue lines: numerical simulations. Red dots: experimental values. Black line: reference model (see [1]).

half width of the plate. This figure can be viewed as a photograph of the plate taken from above the experimental set-up, with the fluid flow going from the left to the right side. The profiles are stationnary, and the error bars plotted in the figure is the standard deviation of the temporal signal recorded at each position in the profile. At low flow velocities, there is little deformation compared to the plate's length (less than 0.05 %); at 10 m/s, the deformation starts to grow, and becomes larger than 0.1 %. As the flow velocity reaches 25 m/s, the deformation has become larger than 1 %; but another instability arises, and the plate starts to flutter (the corresponding measurement is not shown on this figure). Furthermore, above 10 m/s, the plate's profile looses its symmetry. As the flow velocity increases, the plate reaches a static shape of a first mode with a maximum of deflection shifted downstream.

The amplitude of deformation follows two regimes of evolution, as shown in figure 7: at low flow velocities, the plate is deformed with a small amplitude almost constant. Above a certain value of flow velocity, the amplitude grows fast; the trend becomes linear with the square of velocity. In the case of figure 7, the slope obtained by linear regression in the diverged regime is 4 times the slope at low flow velocity (for a variance at 0.85 in both regimes). The critical velocity is obtained by computing the intersection between the two linear regression trends; it marks the transition bewteen the two regimes. In figure 7, the critical velocity is estimated at 9.8 m/s.

EFFECT OF CONFINMENT ON THE CRITICAL VELOCITY

The effect of lateral confinment on the critical velocity is shown in figure 8. As $\frac{D}{L}$ decreases the critical velocity decreases. In fact, as the space between the channel walls and the plate decreases, the efffect of the plate's curvature on the pressure variation is enhanced. The fluid forces increase whereas the elastic forces are constant; therefore the critical velocity is lowered. The 3D numerical simulations give a consistently

higher critical velocity compared to a 2D model and the reference solution [1]. As the other confinment parameter $\frac{C}{L}$ decreases, the critical velocity evolution with $\frac{D}{L}$ gets closer to the 2D models curve which can be seen as the limit case of a plate with inifinite width. The experimental results seem to be between the 3D numerical simulations and the 2D model. However, in the experimental configuration, the actual value of the other confinment parameter is lower than the ones used in the numerical simulation: $\frac{C}{L} = 0.02$. Again, as the lateral confinment $\frac{D}{L}$ decreases, the critical velocity for divergence decreases. The difference bewteen the 3D numerical simulations and experimental data may lay in the absence of friction forces in the 3D potential model, which act alongside the plate as an additional force. This may trigger the divergence instability sooner than expected in terms of fluid velocity. On the contrary, the 2D model underestimates the critical velocity; this may linked to the presence of tension in the experimental set-up, as the streamlined ends do not perform a perfect clamped-clamped boundary condition for the plate. The 2D model also does not take into account the possible presence of non-linearities in the plate's behaviour, such as tension arising due to small deformation neven at small flow velocities.

CONCLUSIONS

These results show the importance of 3D modelling (rather than 2D) in order to predict the critical divergence velocities. Results obtained with the two methods were expected to be different, but the impact of the modelling choice is quantified. For example, the critical velocity with a 3D model is at least three times higher than the velocity computed with a 2D model. This ratio is even higher in extremly confined configurations (small values of $\frac{D}{L}$). Compared to the experimental results, the 3D model overestimates the divergence threshold, whereas a 2D model underestimates it; but more experimental data would be needed in order to confirm this trend. Even if the experimental clamped-clamped boundary conditions seems to be quite good, there may be small tension in the plate even at rest, which tends to shift the divergence threshold to higher flow velocities. However, the influence of lateral confinment follows the same trends in experimental results, and in 2D and 3D models.

REFERENCES

[1] Guo, C. Q., and Païdoussis, M. P., 2000. "Analysis of hydroelastic instabilities of rectangular parallel-plate assemblies". *Journal of Pressure Vessel Technology,* ***122***(4), Mar., pp. 502–508.

[2] Kornecki, A., Dowell, E., and O'Brien, J., 1976. "On the aeroelastic instability of two-dimensional panels in uniform incompressible flow". *Journal of Sound and Vibration,* ***47***(2), pp. 163–178.

[3] Doaré, O., Sauzade, M., and Eloy, C., 2011. "Flutter of an elastic plate in a channel flow: Confinement and finite-size effects". *Journal of Fluids and Structures,* ***27***(1), Jan., pp. 76–88.

[4] *Code_Aster*, http://www.code-aster.org.

[5] Blevins, R. D., 1984. *Formulas for natural frequency and mode shape*. Krieger.